Journal of Alloys and Compounds 1036 (2025) 181653

Contents lists available at ScienceDirect

Journal of Alloys and Compounds

journal homepage: www.elsevier.com/locate/jalcom

Nanoindentation behavior of $Al_{0.3}CoCrFeNi$ high entropy alloy: Experimental study and crystal plasticity finite element simulation

Yingying Wang [a,b], Mingqi Lei [a], Yu Tong [c], Nicolò Grilli [b,*], Yao Yao [a]

[a] School of Mechanics, Civil Engineering and Architecture, Northwestern Polytechnical University, Xi'an 710072, China
[b] School of Electrical, Electronic and Mechanical Engineering, University of Bristol, Bristol BS8 1TR, United Kingdom
[c] CAS Key Laboratory of Magnetic Materials and Devices, and Zhejiang Province Key Laboratory of Magnetic Materials and Application Technology, Ningbo Institute of Materials Technology and Engineering, Chinese Academy of Sciences, Ningbo, China

ARTICLE INFO

Keywords:
Creep
Crystal plasticity finite element method
Electron Backscatter diffraction
High entropy alloy
Nanoindentation

ABSTRACT

The effects of loading rate and grain orientation on the deformation behavior of the $Al_{0.3}CoCrFeNi$ high entropy alloy (HEA) under nanoindentation loading were investigated experimentally and numerically, respectively. Experimental results demonstrated that the nanoindentation creep behavior of the alloy is highly sensitive to the loading rate: a higher loading rate results in smaller displacement during the loading stage and greater creep displacement during the holding stage. This is because, at lower loading rates, creep deformation has sufficient time to develop during the loading stage. X-ray diffraction (XRD) and electron backscatter diffraction (EBSD) were conducted to obtain crystallographic information for input into the crystal plasticity finite element model (CPFEM). A representative volume element (RVE) finite element model of the alloy was reconstructed, and uniaxial tensile simulation was performed to validate the accuracy of the CPFEM and its parameters set. Based on the stress contour of tensile simulation result, 8 representative grain orientations were selected to investigate their influence on nanoindentation deformation using CPFEM. The results indicate that nanoindentation deformation in the HEA is strongly affected by grain orientation. Different grain orientations significantly affect the spatial distribution of shear strain, which in turn affects the morphology and distribution of the pile-up during nanoindentation. A combined analysis of the uniaxial tension and nanoindentation simulations reveals that grains with soft orientations are more prone to stress concentration during polycrystalline deformation and exhibit more pronounced pile-up in the single crystal nanoindentation. The grain exhibiting pronounced stress concentration under uniaxial tensile loading also demonstrates a distinct pile-up morphology and relatively large pile-up height in the nanoindentation simulations. In contrast, the grain located in a low-stress region during tensile loading consistently shows a smaller pile-up height. By incorporating CPFEM into the nanoindentation analysis of HEA, this study not only improves the resolution of micromechanical characterization but also provides a theoretical foundation for elucidating their intrinsic plasticity mechanisms and for designing cross-scale strengthening strategies.

1. Introduction

High-entropy alloys (HEAs), as a new type of multi-principal alloy materials, have attracted widespread attention due to their corrosion resistance [1,2], good thermal stability [3], and excellent mechanical properties [4,5] since they were first proposed by Yeh et al. [6]. These exceptional characteristics provide HEAs with great potential for applications in aerospace, nuclear engineering, and advanced manufacturing. The as-cast $Al_{0.3}CoCrFeNi$ HEA, which has a face-centered cubic (FCC) crystalline structure, exhibits a nominal tensile strength of approximately 300 MPa and an elongation of up to 60 % [7]. It is one of the most extensively studied materials among FCC-structured HEAs. Existing research primarily focuses on its macroscopic deformation behavior [8,9] and employs heat treatment methods such as annealing and aging to control its microstructure for improving mechanical properties [10,11]. Specifically, it was found that the shorter annealing time led to a finer grain size and higher hardness [12]. Thermomechanical processes that include drop casting, followed by homogenizing annealing, cold rolling and recrystallization annealing have been able to produce samples with balanced strength and ductility

* Corresponding author.
E-mail addresses: nicolo.grilli@bristol.ac.uk (N. Grilli), yaoy@nwpu.edu.cn (Y. Yao).

https://doi.org/10.1016/j.jallcom.2025.181653
Received 26 April 2025; Received in revised form 6 June 2025; Accepted 14 June 2025
Available online 15 June 2025

Table 1
Atomic percents and calculated weights of the cast sample.

Elements	Al	Co	Cr	Fe	Ni
at%	6.976	23.256	23.256	23.256	23.256
Weight/g	1.040	7.571	6.678	7.173	7.538

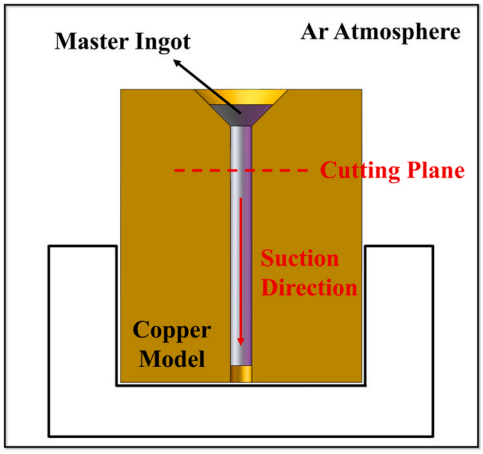

Fig. 1. Schematic illustration of the copper model suction casting process.

at room temperature [12]. Specifically, short-time annealing is used to prevent excessive grain growth, allowing for recrystallization with small grain size.

Previous studies have identified the strain rate dependence and quantified the corresponding stress exponent [8], together with the activation energies of plasticity mechanisms during hot deformation [9]. Twinning deformation leading to high strength and ductility has been identified in $Al_{0.3}$CoCrFeNi, and explained using a combination of experiments and simulations to understand the effect of twin boundary spacing and orientations [13]. The excellent combination of strength and ductility in $Al_{0.3}$CoCrFeNi was mainly ascribed to the combined action of residual dislocations, refined grains, and annealing and deformation twins on the dislocation motion [12]. During large strain deformation, grain reorientation has been identified and correlated with the migration and disappearance of twin boundaries. This mechanism has been explained by the interaction between gliding dislocations and twin boundaries leading to the formation of shear bands, which concentrate the plastic deformation in specific regions of the grain containing twin boundaries [13]. Tensile strength and fracture properties, including fracture surface morphologies, were investigated, showing that $L1_2$ and B2 phases can strengthen the alloy and affect strain to failure, depending on their size [14].

However, there is still a lack of systematic understanding of its deformation behavior at the microscale, especially the underlying deformation mechanisms within individual grains that have yet to be fully revealed. The local deformation characteristics of materials at the micro/nanoscale can be analyzed by nanoindentation, an advanced method of testing mechanical properties [15–17]. At the macroscale, metals and alloys typically exhibit weak strain rate sensitivity under uniaxial tension or compression at room temperature. In contrast, nanoindentation tests reveal a pronounced dependence of the mechanical response on the loading rate [18], and creep behavior is often observed during the holding stage [19,20].

Traditionally, creep is considered a dominant deformation mechanism under high-temperature conditions ($T > 0.5T_m$, T_m is the melting temperature in Kelvin) in macroscopic experiments [21]. However, previous studies have shown that even at room temperature, metals or alloys, including HEAs, still show noticeable creep behavior under nanoindentation [20,22]. Therefore, investigating the nanoindentation deformation and subsequent creep behavior is crucial for understanding the mechanical response of materials at the microscale [23]. This work will systematically investigate the nanoindentation behavior of the $Al_{0.3}$CoCrFeNi HEA under different loading rates. The influence of loading rate on creep characteristics under a constant peak load will be analyzed to further enhance the understanding of its mechanical properties.

Furthermore, the mechanical properties of single crystals are inherently anisotropic [24,25]. In nanoindentation experiments, the indentation scale is significantly smaller than the grain size of coarse-grained $Al_{0.3}$CoCrFeNi HEA, thus probing single grain properties. Consequently, the nanoindentation response is influenced not only by the loading rate but also by the grain orientation. Understanding the effect of grain orientation on nanoindentation deformation is essential for elucidating the underlying plastic deformation mechanisms at the microscale [26]. However, experimentally isolating the influence of grain orientation remains technical challenges due to material heterogeneity and experimental reproducibility. The finite element simulation method represents an accurate analysis tool which can be used with both macroscopic phenomenological models and microscopic physics-based models [27]. Crystal plasticity theory more accurately captures the anisotropic deformation of single crystals, particularly in describing dislocation slip, twinning, and local plastic deformation [28–30]. Accordingly, the crystal plasticity finite element method (CPFEM) can provide a more comprehensive understanding of the influence of grain orientation on deformation mechanisms [31,32].

During nanoindentation deformation, the formation of pile-up morphology is closely related to the accumulation of shear strain, which is, in turn, influenced by grain orientation [33]. Therefore, pile-up morphology can be used as a critical indicator for assessing the effect of grain orientation on local plastic deformation [34], which can be numerically simulated using CPFEM, thus providing insights into the corresponding changes in local stress distribution and underlying deformation mechanisms.

In this work, a combination of experimental techniques and CPFEM is employed to investigate the nanoindentation deformation of $Al_{0.3}$CoCrFeNi HEA. The microstructural features of the alloy are first characterized using X-ray diffraction (XRD) and electron backscatter diffraction (EBSD). Nanoindentation experiments are then conducted to examine creep deformation behavior under different loading rates. Finally, uniaxial tensile simulations are performed to validate the crystal plasticity constitutive model and its parameters. Based on the verified model, nanoindentation simulations are carried out to systematically explore the influence of grain orientation on pile-up morphology and to elucidate the underlying plastic deformation mechanisms.

2. Experiment and results

2.1. Experimental

The $Al_{0.3}$CoCrFeNi HEA was prepared by vacuum arc melting using high-purity (> 99.9 %) elemental raw materials. The bulk raw materials were mechanically polished to remove surface oxides and contaminants, followed by ultrasonic cleaning in alcohol and air drying. The cleaned elements were then accurately weighed using a Mettler Toledo balance with a precision of 10^{-3} g. The atomic percents and corresponding weights of each element are listed in Table 1 for preparing a 30 g master ingot. After placing the weighed elements into a crucible, the chamber was evacuated to below 10^{-4} Pa and backfilled with high-purity argon gas to a pressure of 0.5 atm, with titanium used as a getter to further purify the atmosphere. The samples were remelted at least 4 times and flipped between each melting to improve chemical homogeneity.

The alloy was molded into a cylinder with a diameter of 3 mm using the copper mold suction casting method, as shown in Fig. 1. Samples for nanoindentation testing and EBSD measurement were cut from the cylinder perpendicular to the suction direction, then embedded, ground

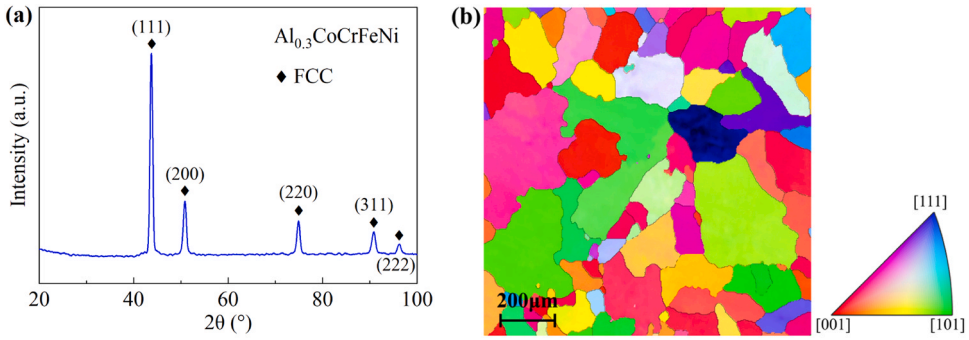

Fig. 2. Microstructure characteristics: (a) the XRD spectrum and (b) EBSD orientation map of the HEA.

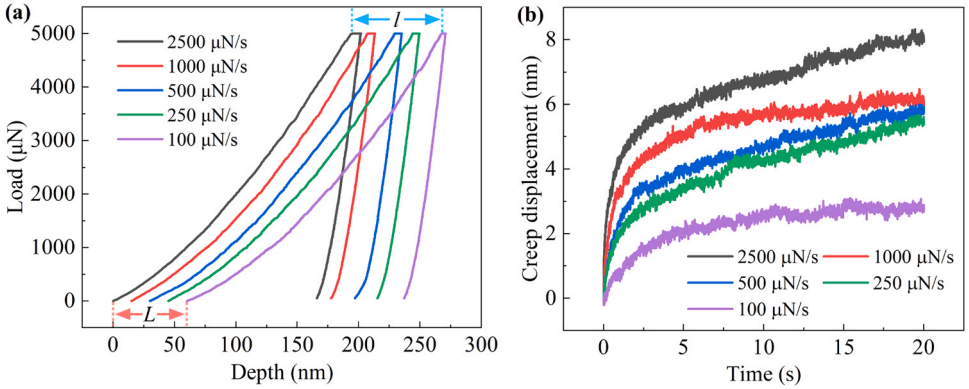

Fig. 3. Nanoindentation creep test results under 5 different loading rates: (a) representative load-displacement curves; (b) creep displacements during the holding stage.

with sandpaper and sequentially polished with diamond suspension to achieve a mirror-like surface suitable for nanoindentation experiments.

The crystalline phase of the alloy was examined using XRD with Cu Kα radiation, over a 2θ range of 20–100° at a scanning speed of 4°/min. The XRD data were analyzed using Jade software (MDI, USA) in combination with the PDF-2 database to identify the phases. EBSD technique was employed to analyze the grain structure and orientation distribution of the alloy, providing realistic microstructural data for CPFEM. Sample preparation for EBSD involved both mechanical polishing and electrolytic polishing to minimize errors caused by residual stress and plastic deformation. EBSD measurements were conducted using a JEOL JSM-7900F scanning electron microscope (SEM) equipped with an Oxford instruments NordlysMax 3 EBSD detector. Data acquisition was performed at an accelerating voltage of 20 kV, with the sample tilted at 70°, and an acquisition frequency of 585.09 Hz.

Nanoindentation tests on the HEA were conducted using TriboIndenter (TI-980) produced by Bruker Hysitron nanoindenter equipped with a standard diamond Berkovich tip. Larsson et al. [35] carried out a systematic analysis with the same shape and size of the Berkovich indenter and demonstrated its effectiveness. The experiments were conducted under load-controlled mode, with a constant load increase. The load limit for each indent was set to 5000 μN and held for 20 s. All tests were carried out at room temperature under ambient atmospheric conditions. The rate sensitivity was investigated through tests at 5 different loading rates, 100 μN/s, 250 μN/s, 500 μN/s, 1000 μN/s, and 2500 μN/s. The unloading rate was fixed 1000 μN/s in all cases. The nanoindentation tests were performed on different grains because the objective was to understand the effect of the loading rate on the force-displacement curve and on the creep behavior.

2.2. Results

Fig. 2 shows the typical XRD pattern and EBSD orientation map of the $Al_{0.3}CoCrFeNi$ HEA. Only diffraction peaks corresponding to a FCC cubic phase are detected in Fig. 2(a), indicating that the as-cast alloy consists of a single-phase solid solution. The EBSD phase map in Fig. 2(b) reveals an average grain size of approximately 106.7 μm, confirming the coarse-grained structure of the alloy.

Fig. 3(a) shows the typical load-displacement curves of the $Al_{0.3}CoCrFeNi$ HEA obtained at five different loading rates, each with a maximum load of 5000 μN. The curves are plotted at equal intervals along the x-axis for better observation. In Fig. 3(a), the capital letter L marks the initial interval of the five curves, while the lowercase letter l indicates their interval along the x-axis after the loading stage. It is obvious that the distance l is larger than L, suggesting that the nanoindentation deformations of the HEA during the loading stage vary with loading rates. Before the holding stage, the decrease in loading rate leads to an increase in the nanoindentation displacement with the same maximum load, revealing the loading rate sensitivity of the HEA.

As shown in Fig. 3(a) and (b), noticeable creep displacements of HEA are clearly observed during the holding stage, even under a load of 5000 μN at room temperature. For traditional uniaxial tensile/compressive creep tests, the stress distribution is relatively homogeneous and there is no stress concentration inside the specimen. Different from traditional creep tests, nanoindentation induces significant strain gradients beneath the indenter, accompanied by a complex stress field [36]. This inhomogeneous deformation leads to a concentration of maximum shear stress near the indenter tip area. Especially in the case of the Berkovich indenter, local stress can exceed the yield strength of the material even under minimal loading. This phenomenon may explain why many high-melting-point metals or alloys exhibit creep behavior at room temperature under nanoindentation load, whereas conventional creep

Table 2
Constitutive parameters of $Al_{0.3}CoCrFeNi$ HEA. [45].

Parameters		Values
Reference shear strain rate $\dot{\gamma}_0/s^{-1}$		0.001
Strain rate sensitivity exponent n		10
Initial hardening modulus h_0/MPa		110
Yield strength τ_0/MPa		85
Saturation stress τ_s/MPa		260
Elasticity modulus	C_{11}/MPa	255,780
	C_{12}/MPa	109,620
	C_{44}/MPa	73,080

tests typically require test temperatures exceeding 0.5 T_m to induce creep deformation [19]. Despite the significant plastic deformation concentrated beneath the indenter, no macroscopic failure of the material is observed under nanoindentation loading.

In traditional creep deformation, the process is typically divided into three stages: primary creep, steady-state creep, and accelerated creep stage, with material failure generally occurring in the third stage. Fig. 3 (b) illustrates creep displacement overtime during the holding stage under five different loading rates. The nanoindentation creep deformation of $Al_{0.3}CoCrFeNi$ HEA includes two stages: initial creep and steady-state creep stage, which are similar to the first two stages of traditional

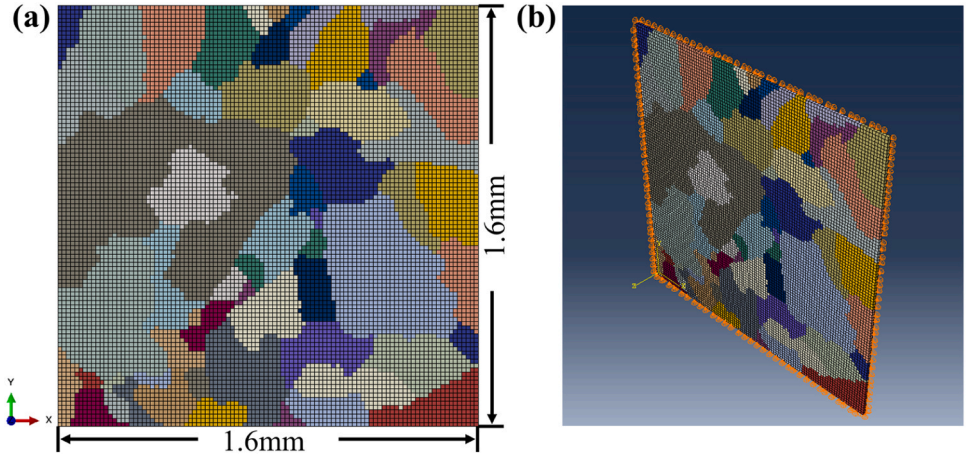

Fig. 4. Finite element model for uniaxial tensile simulation: (a) Finite element model based on the EBSD test; (b) Boundary conditions.

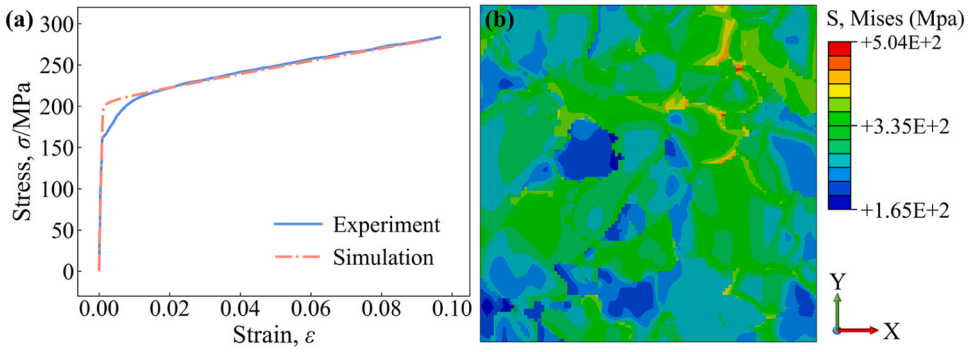

Fig. 5. Simulation results of uniaxial tension: (a) comparison between experimental data and simulation results of macroscopic stress-strain curve under uniaxial tensile loading; (b) Mises stress contour of HEA at 10 % tensile strain.

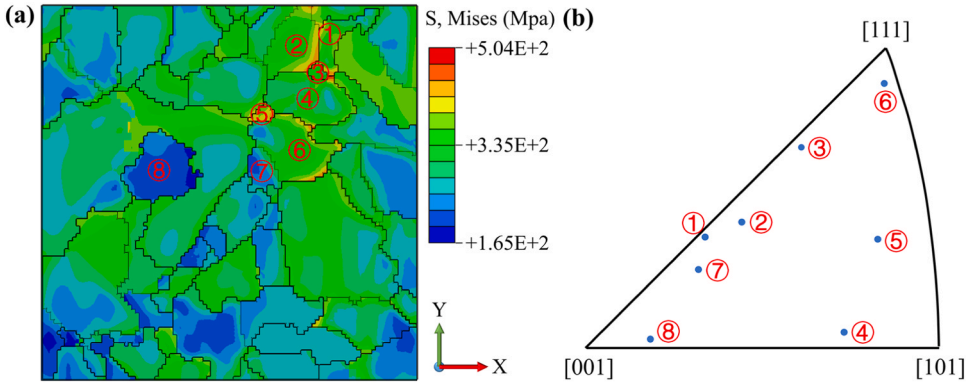

Fig. 6. Selection of grain orientations for nanoindentation simulation: (a) Grain selection based on Mises stress distribution; (b) Orientation distribution of the selected grains along the loading direction, represented in the stereographic triangle.

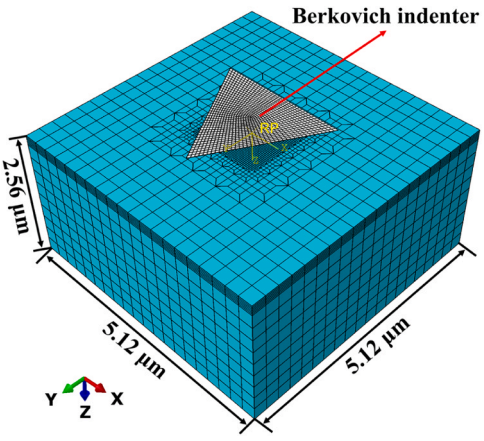

Fig. 7. Nanoindentation crystal plasticity finite element model.

creep deformation. However, no evidence of the third stage was observed.

Furthermore, the magnitude of creep deformation during the holding stage increases with higher loading rates, indicating that the nano-indentation creep behavior of $Al_{0.3}CoCrFeNi$ HEA is affected by the loading rate and exhibits rate dependence. At higher loading rates, creep deformation mainly occurs in the holding stage. This trend is consistent with previous observations in other HEAs [37]. Conversely, at lower loading rates, the extended loading duration involves not only plastic deformation but also creep deformation. Consequently, by the time the holding stage begins, the creep deformation is relatively weak, which can be confirmed by the increase in the length of l in Fig. 3(a).

3. Crystal plasticity finite element method

Although extensive experimental investigations have been conducted on the nano-indentation deformation of HEAs, systematic applications of the CPFEM to investigate their nanomechanical behavior remain scarce. Nanoindentation tests offer valuable localized load–displacement data; however, they provide limited insight into the underlying activation of slip systems and stress-transfer mechanisms beneath the indenter. CPFEM is based on the plastic mechanism dominated by crystal slip and introduces the temperature-strain rate coupled constitutive relationship. It can capture the activation and interaction of dislocations in HEAs and elucidate their modulation effect on macroscopic response. This capability enables quantitatively evaluate the influence of loading rate and grain orientation on the deformation response [38,39].

3.1. Crystal plasticity theory

According to Schmid's law, the slip rate $\dot{\gamma}^\alpha$ on a specific slip system depends solely on the resolved shear stress τ^α, which is related to the externally applied stress σ through the Schmid factor. A power law expression of shear strain rate is used to describe the plastic slip in single crystals [40]:

$$\dot{\gamma}^\alpha = \dot{\gamma}_0 \left(\frac{\tau^\alpha}{g^\alpha}\right)^n \mathrm{sign}(\tau^\alpha), \tag{1}$$

where $\dot{\gamma}_0$ is the reference shear strain rate on slip system α. g^α represents the critical resolved shear stress, which is the minimum shear stress required to activate a slip system. It characterizes the current strength of the slip system. n is the strain rate sensitivity exponent. The Schmid stress of slip system α, τ^α, is the driving force for dislocation slip, and follows Schmid's law:

$$\tau^\alpha = \boldsymbol{\sigma} : \boldsymbol{\mu}^\alpha, \tag{2}$$

where $\boldsymbol{\mu}^\alpha$ is the "Schmid factor" of slip system α, calculated based on the slip direction and the normal to the slip plane:

$$\mu_{ij}^\alpha = \frac{1}{2}\left(s_i^\alpha m_j^\alpha + s_j^\alpha m_i^\alpha\right), \tag{3}$$

where s_i^α and m_i^α are two orthogonal vectors of slip system α: slip direction and the normal vector of slip plane.

The evolution of current strengths g^α represents the strain hardening of each slip system. It evolves with the accumulation of plastic strains:

$$\dot{g}^\alpha = \sum_\beta H_{\alpha\beta}\left|\dot{\gamma}^\beta\right|, \tag{4}$$

where $H_{\alpha\beta}$ are the slip hardening moduli, defining the strain hardening relationship of the slip system β to α. Here, $H_{\alpha\alpha}$ and $H_{\alpha\beta}$ $(\alpha \neq \beta)$ are self and latent hardening modulus, respectively. Peirce, Asaro, and Needleman [41], along with Asaro [42,43], proposed a model for calculating the self-hardening modulus:

$$H_{\alpha\alpha} = h(\Gamma) = h_0 \mathrm{sech}^2\left|\frac{h_0\Gamma}{\tau_s - \tau_0}\right|, \tag{5}$$

where h_0, τ_0 and τ_s are hardening parameters. They are all material-dependent constants. h_0 is the initial hardening modulus; τ_0 is the yield stress, which equals the initial value of slip resistance g_0; τ_s is shear stress at the onset of the saturation of hardening. Γ is defined as the accumulative shear strain over all slip systems:

$$\Gamma = \sum_{\alpha=1}^{N}\int_0^t |\dot{\gamma}^\alpha| \mathrm{d}t. \tag{6}$$

The latent-hardening coefficients are determined from the self-hardening coefficient:

$$H_{\alpha\beta} = qh(\Gamma)(\alpha \neq \beta), \tag{7}$$

where q is a dimensionless constant ranging from 1 to 1.4. For FCC structure, it is assumed to be equivalent for all slip systems due to their high symmetry and similar slip characteristics. In such cases, q is commonly set to 1.0.

This crystal plasticity constitutive model was implemented by Huang [44] in the commercial finite element software ABAQUS using the user-defined material subroutine (UMAT). The increment of plastic shear strain $\Delta\gamma^\alpha$ on slip system α within the time increment Δt is determined by a forward gradient time integration scheme:

$$\Delta\gamma^\alpha = \Delta t\left[(1-\theta)\dot{\gamma}_t^\alpha + \theta\dot{\gamma}_{t+\Delta t}^\alpha\right], \tag{8}$$

where θ is an integration parameter that ranges from 0 to 1. It is recommended to be 0.5 in this model. The shear strain increment $\Delta\gamma^\alpha$ is obtained by solving the N (total number of slip systems) dimensional linear equations:

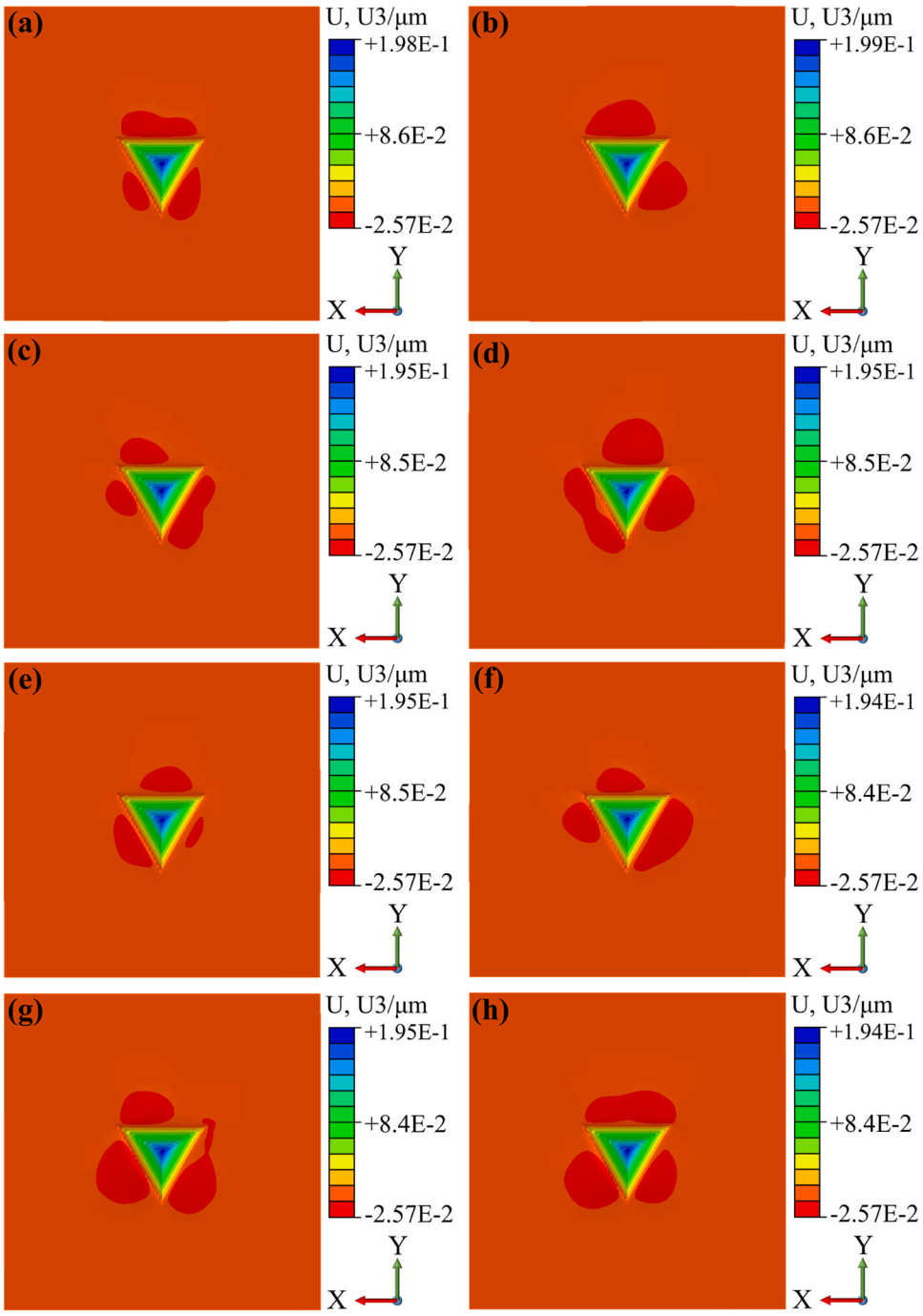

Fig. 8. Nanoindentation pile-up morphologies and displacement field (U3) of different grains obtained from CPFEM simulations ((a)–(h) correspond to grains ①–⑧).

$$\sum_{\beta}\left[\delta_{\alpha\beta}+\theta\Delta t\frac{\partial\dot{\gamma}^{\alpha}}{\partial\tau^{\alpha}}(\mathbf{L}:\boldsymbol{\mu}^{\alpha}+\boldsymbol{\omega}^{\alpha}\boldsymbol{\sigma}-\boldsymbol{\sigma}\boldsymbol{\omega}^{\alpha})\boldsymbol{\mu}^{\beta}-\theta\Delta t\frac{\partial\dot{\gamma}^{\alpha}}{\partial g^{\alpha}}h_{\alpha\beta}sign\left(\dot{\gamma}_{t}^{\beta}\right)\right]\cdot\Delta\gamma^{\beta}$$
$$=\Delta t\dot{\gamma}_{t}^{\alpha}+\theta\Delta t\frac{\partial\dot{\gamma}^{\alpha}}{\partial\tau^{\alpha}}(\mathbf{L}:\boldsymbol{\mu}^{\alpha}+\boldsymbol{\omega}^{\alpha}\boldsymbol{\sigma}-\boldsymbol{\sigma}\boldsymbol{\omega}^{\alpha}):\Delta\boldsymbol{\varepsilon}. \tag{9}$$

Finally, the Newton-Raphson method is employed to solve nonlinear equation systems. The criterion for convergence is based on:

$$\Delta\gamma^{\alpha}-(1-\theta)\Delta t\dot{\gamma}_{t}^{\alpha}-\theta\Delta t\dot{\gamma}_{t+\Delta t}^{\alpha}\leq\varepsilon, \tag{10}$$

where ε is an absolute error.

3.2. Crystal coordinate system transformation

The anisotropy of a grain refers to the difference in its physical properties along different crystallographic directions, which originates from the intrinsic characteristics of its crystal structure, such as lattice type, symmetry, and atomic arrangement. To describe these directional properties, the crystal coordinate system is employed, which aligns with

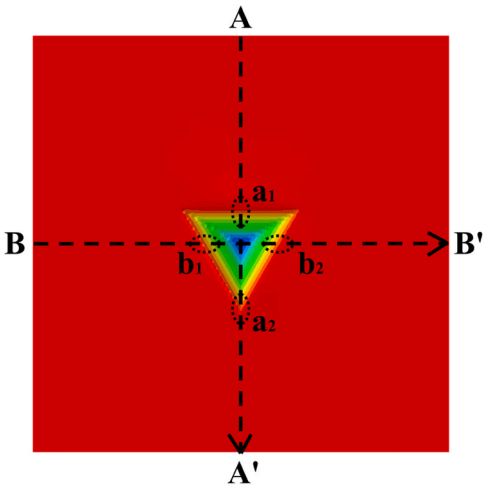

Fig. 9. Displacement extraction paths.

the symmetric axes of the crystal lattice. In contrast, the sample coordinate system is defined based on experimental or processing considerations, typically aligned with the geometric shape of the sample or the loading direction used in mechanical testing. Since the orientation of a grain within a polycrystalline material may not align with the sample coordinate system, the physical properties a_{xyz} described in the crystal coordinate system [*xyz*] must be transformed into A_{XYZ} of the sample coordinate system [*XYZ*] for accurate analysis. This transformation is described by a rotation matrix:

$$A_{XYZ} = \mathbf{R}a_{xyz}, \tag{11}$$

where ***R*** is the rotation matrix. In EBSD analysis, the orientation of each grain is typically represented by a set of Euler angles (φ_1, ϕ, φ_2), following the Bunge convention. Using these Euler angles information, the rotation matrix can be calculated as follows:

$$\mathbf{R} = [\mathbf{l} \quad \mathbf{m} \quad \mathbf{n}] = \begin{bmatrix} \cos\varphi_1\cos\varphi_2 - \sin\varphi_1\cos\varphi_2\cos\phi & -\cos\varphi_1\sin\varphi_2 - \sin\varphi_1\cos\varphi_2\cos\phi & \sin\varphi_1\sin\phi \\ \sin\varphi_1\cos\varphi_2 + \cos\varphi_1\sin\varphi_2\cos\phi & -\sin\varphi_1\sin\varphi_2 + \cos\varphi_1\cos\varphi_2\cos\phi & -\cos\varphi_1\sin\phi \\ \sin\varphi_2\sin\phi & \cos\varphi_2\sin\phi & \cos\phi \end{bmatrix} \tag{12}$$

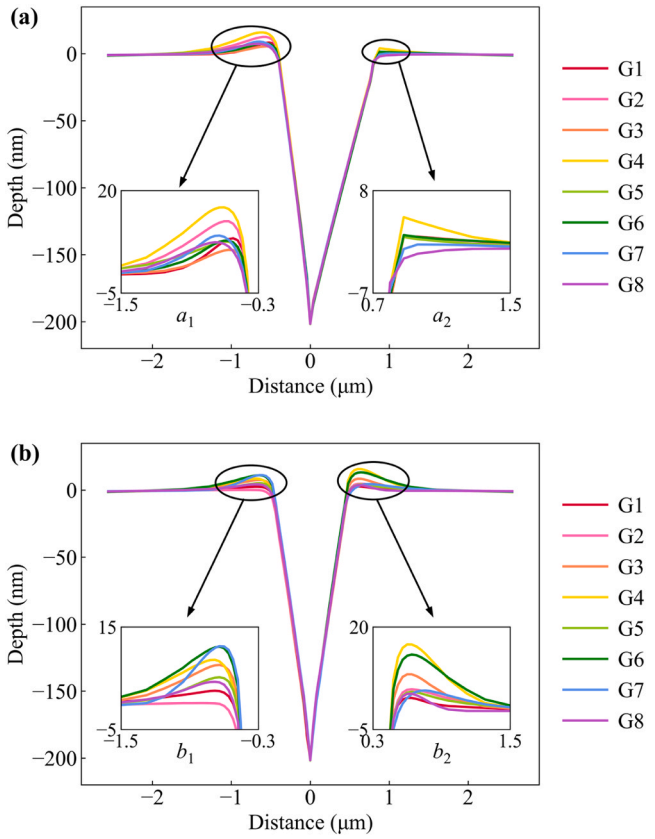

Fig. 10. Path-displacement curves of all grains along different paths: (a) along Path AA'; (b) along Path BB'.

gradients. The CPFEM has been extensively developed and widely applied in nanoindentation simulations of metals and alloys. However, this work represents its first application to the nanoindentation simulation of HEA. Accordingly, certain methods and techniques previously developed for other metallic materials have been adapted in this study. For example, Zaafarani et al. [46] determined the constitutive parameters for nanoindentation simulations of Cu single crystal by fitting the data obtained from uniaxial compression tests. This is possible because CPFEM explicitly account for the interaction between different slip systems that are activated depending on the stress-state, thus making it an ideal technique to predict the mechanical behavior based on calibrations made on a limited set of experiments. Su et al. [38] calibrated the CPFEM parameters for nanoindentation simulations of Mg alloys by fitting the stress-strain curve obtained from the uniaxial tension experiments. This is the motivation for applying this methodology to the current study. Furthermore, the crystal plasticity theory is a physically based constitutive model and have been shown in previous studies to capture the essential features of crystal plasticity in FCC HEAs under different loading conditions. Zhai et al. [45] employed the crystal plasticity model and these parameters to analyze the relationship between fatigue crack initiation and crystal slip deformation for

3.3. Model validation and tensile simulation

XRD analysis confirmed that the crystal structure of $Al_{0.3}CoCrFeNi$ HEA is a single-phase FCC. In FCC crystal, the primary slip systems are associated with the close-packed {111} slip plane family and the ⟨110⟩ slip direction family. Specifically, there are a total of 12 slip systems, all of which are equivalent. Zhai et al. [45] provide a detailed parameter calibration process of $Al_{0.3}CoCrFeNi$ HEA. This study adopts their calibrated values for subsequent numerical simulations. Notably, among the parameters in the crystal plasticity constitutive model, the yield stress determines the initial yield strength of the material, while the initial hardening modulus affects the post-yield hardening rate. A complete list of the material parameters used in the simulations is provided in Table 2.

The CPFEM parameters used in this study were initially calibrated based on uniaxial tensile simulations. Nanoindentation introduces a more complex and highly localized stress state, involving different deformation mechanisms such as higher triaxiality and significant strain

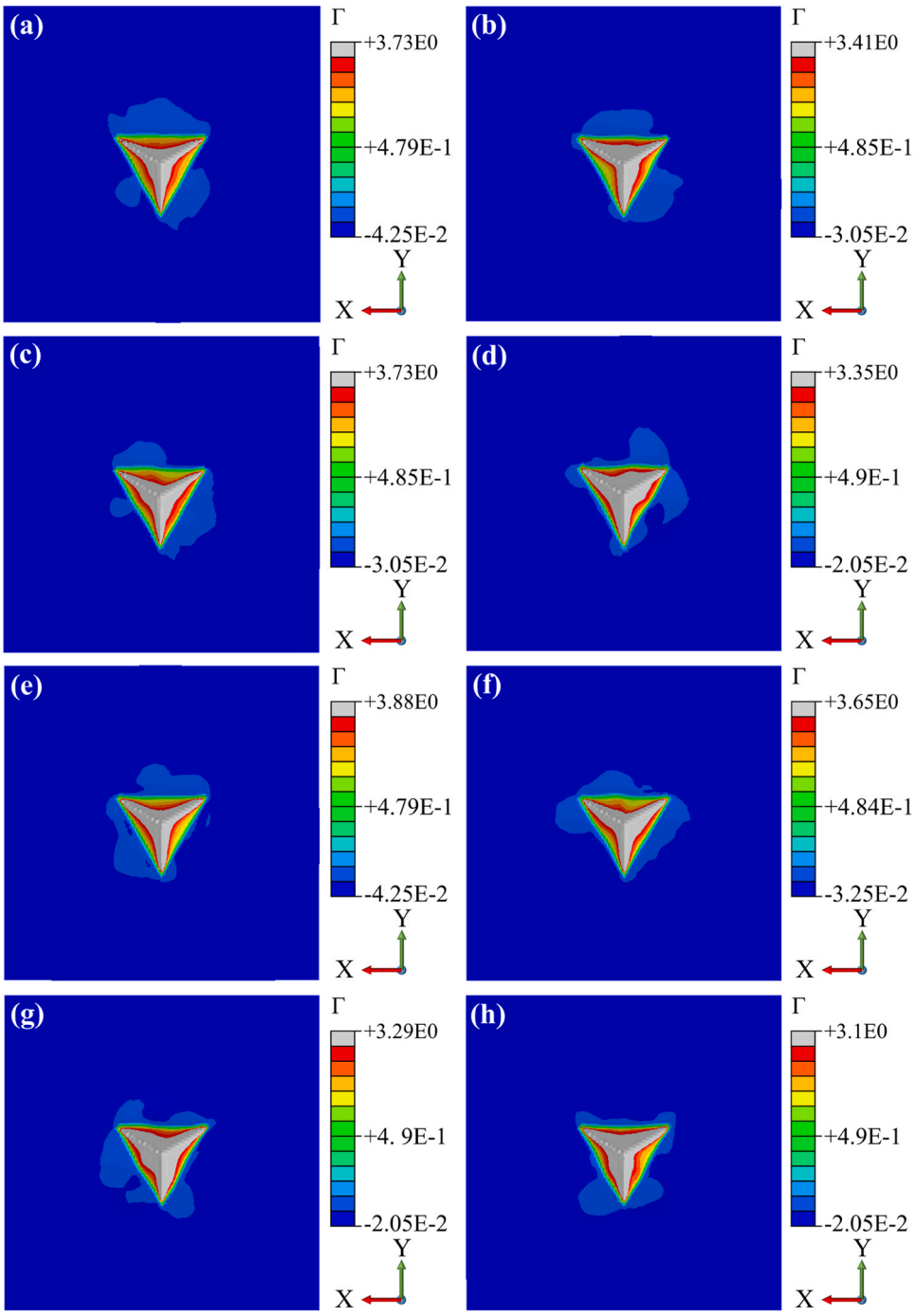

Fig. 11. Cumulative shear strain (Γ) distribution for different grains ((a)–(h) correspond to grains ①–⑧).

$Al_{0.3}$CoCrFeNi HEA.

To validate the accuracy of the constitutive model and its parameters, a quasi-three-dimensional (3D) model of HEA was constructed based on EBSD experimental data. A uniaxial tensile simulation was then conducted. The detailed procedure is as follows: First, the EBSD data obtained from the experiment were imported into DREAM.3D to generate a mesh and reconstruct a representative polycrystalline microstructure. The resulting model retained the geometric and crystallographic characteristics of the actual HEA microstructure. Subsequently, the generated model was imported into ABAQUS, where boundary conditions and load parameters were defined to perform the uniaxial tensile simulation.

The quasi-3D model constructed based on the actual microstructure of HEA is shown in Fig. 4(a). This choice was made to address the effect of variability in mechanical properties given by the different grain orientations. The different grains had different behavior in the tensile simulation, therefore this choice mitigated the effect of variability on model parameter fitting. The model dimensions are 1.6 mm × 1.6 mm × 16 μm. To discretize the domain, the model is meshed into 100 elements along both the x- and y-directions, while only a single element is used in the z-direction. The boundary conditions used in the simulation are shown in Fig. 4(b). Displacement constraints are applied to the three surfaces oriented in the negative directions of the three axes to restrict the normal displacement. A displacement-controlled load with a constant strain rate of 0.001 s^{-1} is applied in the tensile direction (positive direction of the x-axis) to simulate the stress-strain response under

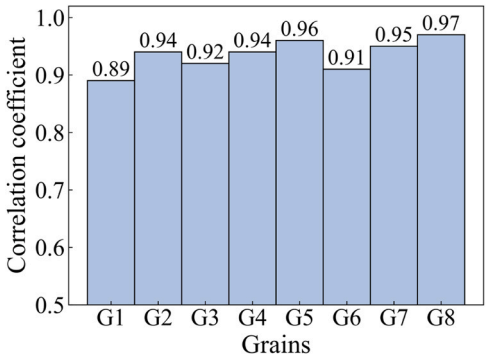

Fig. 12. Correlation coefficient between cumulative shear strain and pile-up morphology across the 8 grains at a_1 region along path AA'.

uniaxial tension.

After the simulation, a Python script is employed for post-processing the result files to extract the macroscopic stress-strain curve. The macroscopic stress $\mathbf{\Sigma}$ and strain $\mathbf{E}$ are obtained by averaging the stress and strain over all elements [46]:

$$\mathbf{\Sigma} = \sum_{i=1}^{N_e} f_i \boldsymbol{\sigma}_i \tag{13}$$

$$\mathbf{E} = \sum_{i=1}^{N_e} f_i \boldsymbol{\varepsilon}_i \tag{14}$$

where f, $\boldsymbol{\sigma}_i$, and $\boldsymbol{\varepsilon}_i$ represent the volume fraction of the ith element in the total model, the stress tensor, and the strain tensor, respectively, while N_e denotes the total number of elements.

Fig. 5(a) presents a comparison between the simulated and experimental macroscopic stress-strain curves for $Al_{0.3}CoCrFeNi$ HEA. It can be seen that the simulation results are in good agreement with the experimental data in terms of the overall trend. Particularly in the elastic deformation and work hardening stages, it can accurately describe the mechanical response of HEA under uniaxial tensile loads. However, a specific deviation is observed between simulation result and experimental data during the yielding stage. This phenomenon is primarily attributed to the limitation of the hardening model, which does not fully capture the complex microscopic deformation mechanism of the alloy [45]. Despite this limitation, the simulation results still demonstrate high accuracy overall, providing effective numerical support for studying the mechanical behavior of HEA. The credibility of the model also supports its application in subsequent nanoindentation simulations.

Fig. 5(b) shows the Mises stress contour of HEA at a tensile strain of 0.1. The result reveals that the pronounced stress heterogeneity within the polycrystalline structure, characterized by a clear contrast between regions of high stress concentration (in red) and regions of lower stress (in blue). This heterogeneity is primarily attributed to differences in grain orientation, grain boundary effects, and variations in the activation of the slip systems. It is well acknowledged that grain boundaries act as barriers to dislocation motion due to the misorientation between adjacent grains. Dislocations tend to accumulate at grain boundaries when their glide planes or directions are not continuous across the boundary, leading to dislocation pile-up and local stress concentrations [47]. This phenomenon underlies the classical Hall-Petch relationship, which correlates reduced grain size with increased yield strength due to the higher density of grain boundaries impeding plastic flow [48]. Due to the anisotropic elastic and plastic responses of differently oriented grains, localized stress gradients emerge. High-stress regions are typically located at grain boundaries, regions with large misorientation, or areas where dislocation motion is restricted, while low-stress regions are more likely to appear in areas where slip is well-developed and dislocation transmission is relatively smooth.

The analysis of the stress contour indicates that grain orientation

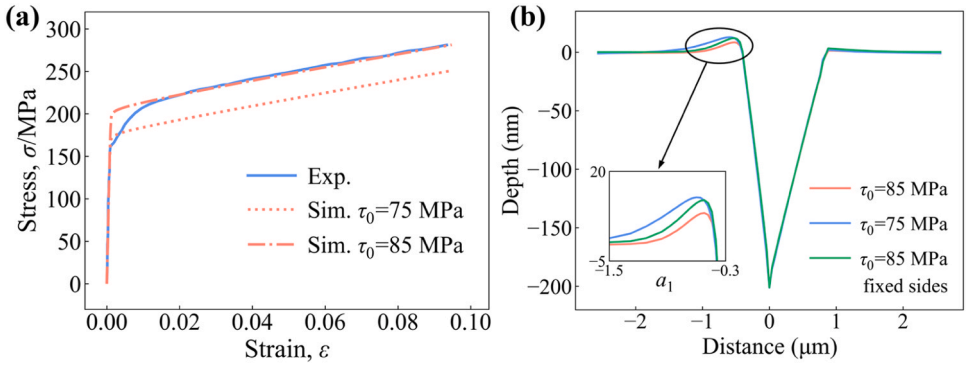

Fig. 13. Simulation results under varying initial yield strength, varied by changing τ_0, using Grain ① as a representative case: (a) stress-strain curves of uniaxial tension; (b) path-displacement curves obtained from nanoindentation simulations.

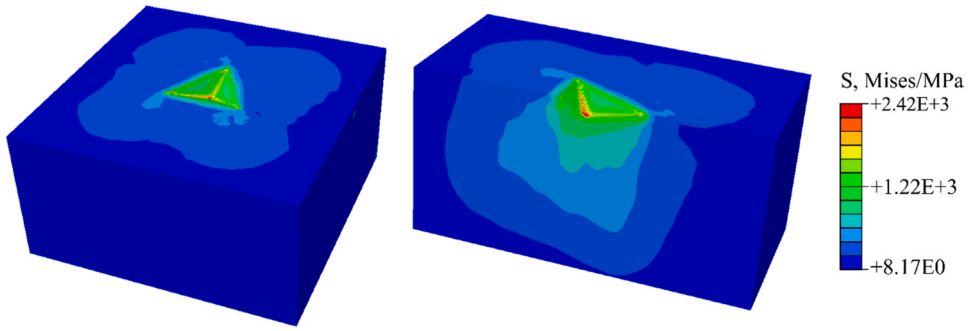

Fig. 14. Mises stress contour of HEA under nanoindentation.

plays a crucial role in the heterogeneity of stress distribution within polycrystalline materials. Different grain orientations influence the preferential activation of local slip systems, resulting in variations in stress concentration and relaxation. Therefore, exploring the relationship between grain orientation and stress distribution is essential for advancing the understanding of the mechanical behavior of polycrystalline materials. In coarse-grained $Al_{0.3}CoCrFeNi$ HEA, the grain size typically ranges from tens to several hundreds of micrometers, which is significantly larger than the contact radius of a Berkovich indenter (approximately 100 nm to 1 μm). Consequently, nanoindentation generally probes within a single grain. In such cases, stress and deformation are governed by elastic anisotropy and slip system characteristics of materials, resulting in orientation-dependent differences in nanoindentation test results.

From the perspective of finite element simulation, CPFEM can accurately capture the microscopic deformation mechanisms by defining the crystal orientation matrix and the activation conditions of the slip systems. Compared with macroscopic phenomenological models, CPFEM offers a significant advantage in quantitatively evaluating the effect of grain orientation on local mechanical responses, making it particularly effective for simulating the heterogeneous deformation of crystalline materials. To deeply understand the effect of grain orientation on nanoindentation behavior, CPFEM was employed to simulate the nanoindentation behavior of $Al_{0.3}CoCrFeNi$ HEA. As illustrated in Fig. 6(a), 8 representative grains were selected based on differences in grain orientation and local stress concentration. The choice of these specific grains was made to understand the variability due to grain orientation within the same region of the sample, given that these grains exhibit a wide range of stress levels. Their orientation distributions along the loading direction are shown in Fig. 6(b) using a stereographic triangle. By simulating the nanoindentation process across these orientations, the pile-up morphology and the locally accumulated shear strain in the nanoindentation region were extracted, thereby quantifying the effect of grain orientation on the plastic deformation during nanoindentation.

4. Nanoindentation simulation

Experimental studies in Section 2.2 have investigated the effect of loading rate on the creep behavior of $Al_{0.3}CoCrFeNi$ HEA. However, experimental approaches have inherent limitations in elucidating deformation mechanisms, as they struggle to control critical parameters independently. In addition, macroscopic phenomenological constitutive models lack the capability to accurately capture the anisotropic deformation behavior of single crystals. To address these limitations, the CPFEM is employed to investigate the nanoindentation deformation behavior and provide insights into the microscopic deformation mechanisms [49–51].

4.1. Finite element model

The average grain size of HEA is three orders of magnitude larger than the nanoindentation depth. As a result, the entire deformation zone induced by indentation remains fully within a single grain. The effect of grain boundaries is negligible in this context and was not considered in the modeling. Therefore, it is physically reasonable to employ a single-crystal finite element model to simulate the nanoindentation deformation of HEA [52]. As shown in Fig. 7, a 3D model was built to simulate the nanoindentation of a single crystal HEA using a Berkovich indenter. The single crystal was modeled as a deformable block with dimensions of $5.12 \times 5.12 \times 2.56\ \mu m^3$ (X × Y × Z), while the Berkovich indenter was defined as a discrete rigid body. The size of the model is large enough to certainly cover the affected area of nanoindentation since the maximum depth of indentation is 200 nm. The deformable block was meshed with linear hexahedral elements (C3D8), and the rigid body was meshed with discrete rigid elements (R3D4). A transition mesh in the region beneath the indenter tip was taken to balance simulation accuracy and computational efficiency. The bottom surface of the specimen was fixed while all the other surfaces were left free.

4.2. Results and discussion

The pile-up phenomenon refers to the localized plastic deformation where materials are extruded upwards around the edge of indenter after nanoindentation due to dislocation movement [53]. Fig. 8 presents the pile-up morphologies and displacement field of different grains obtained from CPFEM simulations. Subfigures (a)–(h) correspond to the simulation results for grains ①–⑧, as defined in Fig. 6. It can be observed that pile-up occurs at all indentation edges, characterized by localized protrusions in the displacement field (red area). The pile-up is primarily distributed around the indentation edge. Under the identical load, single crystals with different grain orientations exhibit variations in pile-up location and morphology, indicating that the plastic response of FCC-structured HEA is highly sensitive to grain orientation [54]. The CPFEM simulations successfully capture the preferential activation of slip systems, dislocation accumulation, and the resulting orientation-dependent pile-up behavior, providing insights into the orientation sensitivity of nanoindentation deformation. Notably, grain ⑤ exhibits the smallest pile-up morphology, whereas both grain ④-characterized by a pronounced stress-concentration zone -and grain ⑧, which experiences comparatively low stresses in the tensile simulation (As shown in Fig. 6(a)), display much larger pile-up features.

To quantitatively analyze the influence of grain orientations on nanoindentation pile-up morphology, the displacement components of the upper surface nodes along the indentation direction were extracted along two predefined paths, AA' and BB', as shown in Fig. 9. The corresponding path-displacement curves are plotted in Fig. 10, where G1–G8 represent the simulation results for grains ①–⑧.

As illustrated in Fig. 10, there are local deformation differences in regions a_1, a_2, b_1, and b_2 near the edge of the indentation along Paths AA' and BB'. The pile-up in region a_2 is notably weaker than in the other three regions. This is consistent with the pile-up positions shown in Fig. 8, where significant pile-up predominantly occurs near the three edges of the indentation, with minimal accumulation near the tip.

The path-displacement curves corresponding to different grains exhibit similar trends within the central indentation zone but begin to diverge near the indentation edges. This divergence highlights the influence of crystallographic orientation, as grains with distinct orientations respond differently to localized plastic deformation due to anisotropic mechanical properties. Furthermore, as shown in the inset of Fig. 10 (a), grain ④ (yellow curve) exhibits the most pronounced pile-up behavior in region a_1, with the highest pile-up height, whereas grain ③ (orange curve) displays a relatively lower pile-up height in the same region. Comparing this with the pile-up morphology in Fig. 8, grain ④ also exhibits the biggest pile-up shape in region a_1, while grain ③ shows the smallest one in the same area. This consistency confirms that the pile-up depth can, to some extent, reflect the overall pile-up morphology.

Fig. 10 (b) further investigates the pile-up characteristics along Paths BB'. Different from Paths AA' in Fig. 10 (a), Path BB' is perpendicular to the symmetry axis of the triangular indentation and passes through two of its edges. Consequently, the indentation deformation along this path is symmetric with respect to the axis $x = 0$. The pile-up height variations near the indentation edges are primarily attributed to grain orientation differences. For example, grains ⑥ (green curve) and ⑦ (blue curve) exhibit higher pile-up heights in region b_1, while grains ④ and ⑥ show greater pile-up heights in region b_2.

By correlating these findings with the stress distribution shown in Fig. 5(b) and Fig. 6(a), it is evident that grain ④ corresponds to a stress concentration region in the uniaxial tensile simulation. Correspondingly, in Fig. 10, grain ④ consistently exhibits a higher pile-up height, indicating that significant pile-up tends to occur in soft-oriented grains.

These grains, characterized by lower critical resolved shear stress, are more susceptible to slip activation and thus play a dominant role in localized deformation and stress concentration during polycrystalline plasticity. In contrast, grain ⑧, which is located in a low-stress region in Fig. 6(a), consistently exhibits a lower pile-up height, identifying it as a hard-oriented grain. This suggests that dislocation motion is more difficult to initiate in hard-oriented grain, leading to less plastic deformation in the coordinated deformation of polycrystals.

The evolution of pile-up morphology under different grain orientations indicates the critical role of crystallographic anisotropy in governing the plastic deformation behavior of single crystals. By analyzing the cumulative shear strain, the plastic flow characteristics associated with different grain orientations can be quantitatively revealed, providing critical insights into the understanding of the mechanical behavior of materials. Fig. 11 presents the simulated cumulative shear strain distributions on all slip systems around the nanoindentation region for 8 different grains. Comparing it with Fig. 8, it reveals that pile-up predominantly occurs in regions with concentrated shear strain, suggesting that the shear strain field plays a key role in the formation of pile-up. Due to anisotropic mechanical properties, grains with different crystallographic orientations activate different numbers and combinations of slip systems under identical loading conditions. This variation leads to differences in shear strain localization, ultimately affecting the morphology and distribution of pile-up. Therefore, the pile-up morphology essentially reflects the differences in internal plastic flow between grains.

To quantitatively strengthen this argument, correlation coefficients between cumulative shear strain and the pile-up depth were calculated within the a_1 region along the path AA' for each grain. As shown in Fig. 12, all 8 grains exhibit high correlation coefficients (ranging from 0.89 to 0.97), including a strong and consistent positive correlation between accumulative shear strain and pile-up morphology. This statistical evidence strengthens the role of shear strain as a key driver in the development of pile-up features.

Overall, the results from CPFEM simulations indicate that grain orientation significantly influences the distribution of plastic deformation around the nanoindentation. The deformation at the indentation center is primarily dominated by the indentation load, whereas the deformation distribution at the indentation edges is more strongly affected by grain orientation. The simulation results based on CPFEM contribute to a deeper understanding of the microscopic deformation mechanisms of HEAs under small-scale mechanical loading. Furthermore, these findings provide theoretical guidance for analyzing the anisotropic deformation of single-crystal materials and offer valuable insights for optimizing the microstructure of alloys at the nanoscale.

To understand the effect of plasticity model parameters on the nanoindentation predictions and to quantify the deviation between tensile experiment and simulation, we repeated the simulations with a different value of the initial yield strength parameter τ_0. A value of 75 MPa has been used, which is 10 MPa lower than the reference value in Table 2. The comparison with the experimental tensile test is shown in Fig. 13 (a), demonstrating that the reference parameter $\tau_0 = 85$MPaoverestimates the stress up to about 1 % strain, while the value $\tau_0 = 75$MPaunderestimates the stress by about 31 MPa, showing that $\tau_0 = 85$MPais more appropriate at large strain. To understand the effect of this parameter on the nanoindentation predictions, an analysis of the pile-up effect for the two different τ_0 has been added in Fig. 13 (b). It turns out that the pile-up depth differs by 4.3 nm, while the maximum stress is lower by 18 MPa. This demonstrates that a variability of about 30 % on the pile-up depth is present; however, due to the relatively large strain near the indent, the value $\tau_0 = 85$MPa is more appropriate, as it matches the stress at large strain in the uniaxial test.

The CPFEM has been extensively developed and widely applied in nanoindentation simulations of metals and alloys. According to the literature, the dimensions of the specimen should be 10 times thicker than the maximum depth of indentation in order to avoid the influence from the substrate [33,38,55]. This was the motivation to choose a substrate with a thickness 2.56 microns in the present study, given that the indentation depth is 200 nm. Thus, we believe that the boundary conditions do not affect the local plastic deformation. To further confirm that the penetration depth and resulting stress field are not affected by the boundary conditions, a plot of the stress field and a slice of the geometry is made for better visualization, as shown in Fig. 14. It is evident that the magnitude of the Mises stress field near the bottom surface is almost 3 orders of magnitude smaller than the maximum stress below the indenter tip, demonstrating that boundary conditions are applied far enough from the load region. Therefore, the boundary conditions used are not strongly affecting the results near the indent, including the results about the pile-up.

To evaluate the influence of boundary conditions on the simulation results, additional simulations were conducted by applying constraints on the lateral surfaces perpendicular to the X and Y axes. Specifically, these boundary conditions restricted displacement normal to the respective surfaces. The corresponding simulation results are shown in Fig. 13 (b): the difference in pile-up depth turns out to be smaller than the difference observed by decreasing the τ_0 parameter by 10 MPa.

5. Conclusions

In this work, the nanoindentation behavior of $Al_{0.3}$CoCrFeNi HEA was investigated through a combination of experimental studies and CPFEM. First, microstructural characterization techniques, including XRD and EBSD, confirmed that the $Al_{0.3}$CoCrFeNi HEA exhibits a single-phase, coarse-grained FCC structure. This experiment supports the establishment of a nanoindentation model and the identification of active slip systems in the crystal plasticity framework. The Euler angle data obtained from EBSD experiments were further utilized to reconstruct the polycrystalline tensile model. By comparing the macroscopic stress-strain curve of uniaxial tensile simulation results with experimental data, the parameters of the crystal plasticity constitutive model, together with their uncertainty, were found. Subsequently, the nanoindentation experiments explored the effect of loading rate on the nanoindentation creep behavior of HEA at room temperature. Finally, the validated constitutive model was used to establish a single crystal nanoindentation model. The influence of grain orientation on pile-up morphology during nanoindentation was systematically analyzed using CPFEM. The conclusions are as follows:

(1) The nanoindentation creep behavior of $Al_{0.3}$CoCrFeNi HEA exhibits strong sensitivity to the loading rate. During the loading stage, a decrease in loading rate results in greater displacement at the same peak load. During the holding stage, creep displacement increases with an increasing loading rate in the loading stage.
(2) This work is the first application of CPFEM in the simulation of HEA nanoindentation deformation. Based on the well-established CPFEM frameworks for conventional metals, including parameter calibration strategies, single-crystal FEM, and boundary condition setups, this study applies key modeling techniques in the context of HEA, ensuring consistency and physical relevance in the simulation of nanoindentation behavior.
(3) Grain orientation has a significant influence on the nanoindentation behavior of HEA. The pile-up morphology of nanoindentations varies considerably depending on the grain orientation.
(4) The locations of pile-up formation coincide with regions of high cumulative shear strain. The shear strain field plays a critical role in the formation of pile-up. Differences in grain orientation led to significant variations in the spatial distribution of shear strain, thereby influencing the morphology and distribution of pile-up.

In summary, the mechanical response of single-crystal and polycrystalline materials under various loading conditions can be accurately

captured using CPFEM. The CPFEM provides insight into the shear strain field of materials during nanoindentation deformation and reveals the physical mechanisms underlying the differences in pile-up morphology across different grain orientations.

Limitations of the developed model include that the mechanical behavior near grain boundaries was not directly compared with experimental observations, the hardening model may only approximately represent complex stress states, and slip gradients were not considered in the prediction of pile-ups.

CRediT authorship contribution statement

Mingqi Lei: Methodology, Data curation. **Yu Tong:** Methodology, Conceptualization. **Nicolò Grilli:** Writing – review & editing, Supervision, Software, Methodology. **Yao Yao:** Writing – review & editing, Supervision, Funding acquisition, Conceptualization. **Yingying Wang:** Writing – review & editing, Writing – original draft, Visualization, Software, Methodology, Investigation, Formal analysis, Data curation, Conceptualization.

Declaration of Competing Interest

The authors declare that they have no conflict of interest.

Acknowledgements

This work was supported by the Innovation Capability Support Program of Shaanxi (Program no. 2022TD-05), the Shaanxi "Sanqin Scholar" Innovation Team (Program no. 2022), the "Scientists + Engineers" Team Construction Project of Qinchuangyuan, Shaanxi Province (Grant no. 2022KXJ-094), and Technology Innovation Leading Program of Shaanxi (Program no. 2023).

Data availability

Data will be made available on request.

References

[1] Y. Fu, J. Li, H. Luo, C.W. Du, X.G. Li, Recent advances on environmental corrosion behavior and mechanism of high-entropy alloys, J. Mater. Sci. Technol. 80 (2021) 217–233, https://doi.org/10.1016/j.jmst.2020.11.044.
[2] Y. Yang, Y. Dong, S. Liu, S. Duan, C. Li, P. Zhang, A novel AlCo1.2Cr0.8FeNi2.1 eutectic high entropy alloy with excellent corrosion resistance, J. Alloy. Compd. 998 (2024) 175006, https://doi.org/10.1016/j.jallcom.2024.175006.
[3] C. He, X.L. Qiu, D.M. Yu, S.S. Zhao, H.X. Guo, G. Liu, X.H. Gao, Greatly enhanced solar absorption via high entropy ceramic AlCrTaTiZrN based solar selective absorber coatings, J. Mater. 7 (2021) 460–469, https://doi.org/10.1016/j.jmat.2020.11.010.
[4] S. Liu, M.C. Gao, P.K. Liaw, Y. Zhang, Microstructures and mechanical properties of AlxCrFeNiTi0.25 alloys, J. Alloy. Compd. 619 (2015) 610–615, https://doi.org/10.1016/j.jallcom.2014.09.073.
[5] R. Feng, C. Zhang, M.C. Gao, Z. Pei, F. Zhang, Y. Chen, D. Ma, K. An, J. D. Poplawsky, L. Ouyang, Y. Ren, J.A. Hawk, M. Widom, P.K. Liaw, High-throughput design of high-performance lightweight high-entropy alloys, Nat. Commun. 12 (2021) 4329, https://doi.org/10.1038/s41467-021-24523-9.
[6] J.W. Yeh, S.K. Chen, S.J. Lin, J.Y. Gan, T.S. Chin, T.T. Shun, C.H. Tsau, S.Y. Chang, Nanostructured high-entropy alloys with multiple principal elements: novel alloy design concepts and outcomes, Adv. Eng. Mater. 6 (2004) 299–303, https://doi.org/10.1002/adem.200300567.
[7] T.T. Shun, Y.C. Du, Microstructure and tensile behaviors of FCC Al0.3CoCrFeNi high entropy alloy, J. Alloy. Compd. 479 (2009) 157–160, https://doi.org/10.1016/j.jallcom.2008.12.088.
[8] Y. Tong, J.C. Qiao, Y. Yao, The constitutive model and threshold stress for characterizing the deformation mechanism of Al0.3CoCrFeNi high entropy alloy, Mater. Sci. Eng. A 730 (2018) 137–146, https://doi.org/10.1016/j.msea.2018.05.109.
[9] M. Patnamsetty, S. Ghosh, M.C. Somani, P. Peura, Characterization of hot deformation behavior of Al0.3CoCrFeNi high-entropy alloy and development of processing map, J. Alloy. Compd. 914 (2022) 165341, https://doi.org/10.1016/j.jallcom.2022.165341.
[10] B. Gwalani, V. Soni, M. Lee, S. Mantri, Y. Ren, R. Banerjee, Optimizing the coupled effects of Hall-Petch and precipitation strengthening in a Al 0.3 CoCrFeNi high entropy alloy, Mater. Des. 121 (2017) 254–260, https://doi.org/10.1016/j.matdes.2017.02.072.
[11] Y. Zhao, Z. Chen, K. Yan, S. Naseem, W. Le, H. Zhang, W. Lu, An investigation on the microstructure and mechanical properties of Al0.3CoCrFeNi high entropy alloy with a heterogeneous microstructure, Mater. Sci. Eng. A 838 (2022) 142759, https://doi.org/10.1016/j.msea.2022.142759.
[12] X. Wang, Z. Zhang, Z. Wang, X. Ren, Excellent tensile property and its mechanism in Al0.3CoCrFeNi high-entropy alloy via thermo-mechanical treatment, J. Alloy. Compd. 897 (2022) 163218, https://doi.org/10.1016/j.jallcom.2021.163218.
[13] T.N. Vu, V.T. Pham, T.H. Fang, Effects of structure and strain rate on deformation mechanism of twin lamellar Al0.3CoCrFeNi alloys, J. Alloy. Compd. 954 (2023) 170174, https://doi.org/10.1016/j.jallcom.2023.170174.
[14] S. Song, X. Wang, Z. Zhang, X. Ren, Investigation on effect of L12 and B2 phases on tensile properties and mechanisms of Al0.3CoCrFeNi high entropy alloy through aging treatment, J. Alloy. Compd. 1010 (2025) 177435, https://doi.org/10.1016/j.jallcom.2024.177435.
[15] Y. Sun, P. Chen, L. Liu, M. Yan, X. Wu, C. Yu, Z. Liu, Local mechanical properties of Al CoCrCuFeNi high entropy alloy characterized using nanoindentation, Intermetallics 93 (2018) 85–88, https://doi.org/10.1016/j.intermet.2017.11.010.
[16] H. Zhang, H. Huang, C. Wang, H. Zhang, H. Wu, H. Zhao, Nanoindentation behaviors of the AlCoCrFeNi2.1 eutectic high-entropy alloy: the effects of crystal structures, J. Alloy. Compd. 1008 (2024) 176535, https://doi.org/10.1016/j.jallcom.2024.176535.
[17] H. Zhai, W. Zhang, X. Si, B. Yao, Z. Wu, Z. Li, X. Ma, F. Zhu, K. Ma, W. Dang, W. Fan, Z. Wang, Microstructure-sensitive plastic deformation behavior of dual-phase Al0.6CoCrFeNi high entropy alloys, J. Alloy. Compd. Commun. 6 (2025) 100073, https://doi.org/10.1016/j.jacomc.2025.100073.
[18] L. Tian, Z.M. Jiao, G.Z. Yuan, S.G. Ma, Z.H. Wang, H.J. Yang, Y. Zhang, J.W. Qiao, Effect of strain rate on deformation behavior of AlCoCrFeNi high-entropy alloy by nanoindentation, J. Mater. Eng. Perform. 25 (2016) 2255–2260, https://doi.org/10.1007/s11665-016-2082-8.
[19] Y. Ma, G.J. Peng, D.H. Wen, T.H. Zhang, Nanoindentation creep behavior in a CoCrFeCuNi high-entropy alloy film with two different structure states, Mater. Sci. Eng. A 621 (2015) 111–117, https://doi.org/10.1016/j.msea.2014.10.065.
[20] D.H. Lee, M.Y. Seok, Y. kai Zhao, I.C. Choi, J. yang He, Z. Lu, J.-Y. Suh, U. Ramamurty, M. Kawasaki, T.G. Langdon, J. Jang, Spherical nanoindentation creep behavior of nanocrystalline and coarse-grained CoCrFeMnNi high-entropy alloys, Acta Mater. 109 (2016) 314–322, https://doi.org/10.1016/j.actamat.2016.02.049.
[21] M.G. Jo, J.Y. Suh, M.Y. Kim, H.J. Kim, W.S. Jung, D.I. Kim, H.N. Han, High temperature tensile and creep properties of CrMnFeCoNi and CrFeCoNi high-entropy alloys, Mater. Sci. Eng. A 838 (2022) 142748, https://doi.org/10.1016/j.msea.2022.142748.
[22] S. Zhu, Y. Wu, S. Hong, J. Cheng, Z. Wei, B. Zhang, Room temperature nanoindentation creep behavior of CoNiCrMo-based high entropy amorphous alloy coatings prepared by HVAF, Intermetallics 163 (2023) 108076, https://doi.org/10.1016/j.intermet.2023.108076.
[23] S. Sinha, R.A. Mirshams, T. Wang, S.S. Nene, M. Frank, K. Liu, R.S. Mishra, Nanoindentation behavior of high entropy alloys with transformation-induced plasticity, Sci. Rep. 9 (2019) 6639, https://doi.org/10.1038/s41598-019-43174-x.
[24] A. Raturi, K. Biswas, N.P. Gurao, Elastic and plastic anisotropy in a refractory high entropy alloy utilizing combinatorial instrumented indentation and electron backscatter diffraction, J. Alloy. Compd. 896 (2022) 162902, https://doi.org/10.1016/j.jallcom.2021.162902.
[25] P. Fan, N.K. Katiyar, M. Arshad, M. Bai, H. Mao, S. Goel, Anisotropic plasticity mechanisms in a newly synthesised high entropy alloy investigated using atomic simulations and nanoindentation experiments, J. Alloy. Compd. 970 (2024) 172541, https://doi.org/10.1016/j.jallcom.2023.172541.
[26] T. Chen, L. Tan, Z. Lu, H. Xu, The effect of grain orientation on nanoindentation behavior of model austenitic alloy Fe-20Cr-25Ni, Acta Mater. 138 (2017) 83–91, https://doi.org/10.1016/j.actamat.2017.07.028.
[27] Y. Su, C. Zambaldi, D. Mercier, P. Eisenlohr, T.R. Bieler, M.A. Crimp, Quantifying deformation processes near grain boundaries in α titanium using nanoindentation and crystal plasticity modeling, Int. J. Plast. 86 (2016) 170–186, https://doi.org/10.1016/j.ijplas.2016.08.007.
[28] Y. Wang, Y. Yao, A multi-scale constitutive model for analyzing the tensile deformation of eutectic high-entropy alloys, Acta Mech. 236 (2025) 241–257, https://doi.org/10.1007/s00707-024-04144-1.
[29] N. Grilli, A.C.F. Cocks, E. Tarleton, A phase field model for the growth and characteristic thickness of deformation-induced twins, J. Mech. Phys. Solids 143 (2020) 104061, https://doi.org/10.1016/j.jmps.2020.104061.
[30] Y. Wang, N. Grilli, M. Salvini, Y. Yao, Microscale deformation, residual stress and fracture behavior of additively manufactured alpha-Ti: combined crystal plasticity and phase-field damage modeling, Comput. Mater. Sci. 252 (2025) 113767, https://doi.org/10.1016/j.commatsci.2025.113767.
[31] B. Yin, X. Xue, B. Tang, W.Y. Wang, H. Kou, J. Li, Experiments and crystal plasticity simulations for the deformation behavior of nanoindentation: application to the α2 phase of TiAl alloy, Mater. Sci. Eng. A 831 (2022) 142283, https://doi.org/10.1016/j.msea.2021.142283.
[32] B. Yin, X. Xue, M. Zhang, T. Deng, J. Li, B. Tang, Parameter identification and pileup behavior of TiAl alloy through nanoindentation and crystal plasticity simulation, J. Alloy. Compd. 948 (2023) 169743, https://doi.org/10.1016/j.jallcom.2023.169743.
[33] F. Han, B. Tang, H. Kou, J. Li, Y. Feng, Experiments and crystal plasticity finite element simulations of nanoindentation on Ti–6Al–4V alloy, Mater. Sci. Eng. A 625 (2015) 28–35, https://doi.org/10.1016/j.msea.2014.11.090.

[34] Z. Zhang, Q. Yan, Y. Zhang, H. Wang, Z. Tong, X. Jiang, New insights into the deformation mechanism of orientation-dependent nanoindentation behaviours, Tribol. Int. 200 (2024) 110112, https://doi.org/10.1016/j.triboint.2024.110112.
[35] P.-L. Larsson, A.E. Giannakopoulos, E. SÖderlund, D.J. Rowcliffe, R. Vestergaard, Analysis of Berkovich indentation, Int. J. Solids Struct. 33 (1996) 221–248, https://doi.org/10.1016/0020-7683(95)00033-7.
[36] W.B. Li, J.L. Henshall, R.M. Hooper, K.E. Easterling, The mechanisms of indentation creep, Acta Metall. et Mater. 39 (1991) 3099–3110, https://doi.org/10.1016/0956-7151(91)90043-Z.
[37] Y. Sun, Y. Huo, W. Yu, Z. Yan, Z. Wang, Z. Li, Z. Wang, H. Chen, A. Jiang, X. Wang, Microstructure and nanoindentation creep behavior of NiAlCrFeMo high-entropy alloy, J. Alloy. Compd. 1020 (2025) 179330, https://doi.org/10.1016/j.jallcom.2025.179330.
[38] H. Su, G. Tian, Y. Li, S. Wang, C. Xue, X. Feng, J. Wang, Breaking the stiffness limit of Mg alloys by forming hard AlX particles and activating non-basal slip, J. Alloy. Compd. 944 (2023) 169249, https://doi.org/10.1016/j.jallcom.2023.169249.
[39] T.J. Gao, D. Zhao, T.W. Zhang, T. Jin, S.G. Ma, Z.H. Wang, Strain-rate-sensitive mechanical response, twinning, and texture features of NiCoCrFe high-entropy alloy: experiments, multi-level crystal plasticity and artificial neural networks modeling, J. Alloy. Compd. 845 (2020) 155911, https://doi.org/10.1016/j.jallcom.2020.155911.
[40] R.J. Asaro, A. Needleman, Overview no. 42 Texture development and strain hardening in rate dependent polycrystals, Acta Met. 33 (1985) 923–953, https://doi.org/10.1016/0001-6160(85)90188-9.
[41] D. Peirce, R.J. Asaro, A. Needleman, An analysis of nonuniform and localized deformation in ductile single crystals, Acta Met. 30 (1982) 1087–1119, https://doi.org/10.1016/0001-6160(82)90005-0.
[42] R.J. Asaro, Micromechanics of crystals and polycrystals, in: J.W. Hutchinson, T. Y. Wu (Eds.), Advances in Applied Mechanics, Elsevier, 1983, pp. 1–115, https://doi.org/10.1016/S0065-2156(08)70242-4.
[43] R.J. Asaro, Crystal plasticity, J. Appl. Mech. 50 (1983) 921–934, https://doi.org/10.1115/1.3167205.
[44] Y. Huang, A User-material Subroutine Incorporating Single Crystal Plasticity in the Abaqus Finite Element Program, Division of Applied Sciences, Harvard University, Cambridge, MA, 1991.
[45] H. Zhai, J. Jiang, W. Zhang, Q. Zhang, X. Ma, S. Wang, Z. Li, W. Qiu, C. Xiao, H. Lin, Microstructure sensitivity of the low cycle fatigue crack initiation mechanisms for the Al0.3CoCrFeNi high entropy alloy: in-situ SEM study and crystal plasticity simulation, Int. J. Fatigue 176 (2023) 107871, https://doi.org/10.1016/j.ijfatigue.2023.107871.
[46] N. Zaafarani, D. Raabe, R.N. Singh, F. Roters, S. Zaefferer, Three-dimensional investigation of the texture and microstructure below a nanoindent in a Cu single crystal using 3D EBSD and crystal plasticity finite element simulations, Acta Mater. 54 (2006) 1863–1876, https://doi.org/10.1016/j.actamat.2005.12.014.
[47] Y. Wang, J. Wang, M. Lei, Y. Yao, A crystal plasticity coupled damage constitutive model of high entropy alloys at high temperature, Acta Mech. Sin. 38 (2022) 122116, https://doi.org/10.1007/s10409-022-22116-x.
[48] Z. Shen, R.H. Wagoner, W.A.T. Clark, Dislocation and grain boundary interactions in metals, Acta Metall. 36 (1988) 3231–3242, https://doi.org/10.1016/0001-6160(88)90058-2.
[49] N. Hansen, Hall–Petch relation and boundary strengthening, Scr. Mater. 51 (2004) 801–806, https://doi.org/10.1016/j.scriptamat.2004.06.002.
[50] Y. Zhou, Q. Fan, X. Liu, D. Wang, X. Zhu, Experimental study and crystal plasticity finite element simulations of nano-indentation-induced lattice rotation and the underlying mechanism in TC6 single α-grain, Mater. Des. 188 (2020) 108423, https://doi.org/10.1016/j.matdes.2019.108423.
[51] H. Su, J. Wang, C. Liu, C. Yan, G. Tian, Z. Yang, C. Xue, X. Yang, Q. Li, X. Li, Y. Miao, Orientation dependence of intracrystalline and grain boundary deformation behavior in Mg-2Y using nanoindentation and CPFEM, J. Alloy. Compd. 994 (2024) 174688, https://doi.org/10.1016/j.jallcom.2024.174688.
[52] C. Zambaldi, Y. Yang, T.R. Bieler, D. Raabe, Orientation informed nanoindentation of α-titanium: indentation pileup in hexagonal metals deforming by prismatic slip, J. Mater. Res. 27 (2012) 356–367, https://doi.org/10.1557/jmr.2011.334.
[53] M.A. Mattucci, I. Cherubin, P. Changizian, T. Skippon, M.R. Daymond, Indentation size effect, geometrically necessary dislocations and pile-up effects in hardness testing of irradiated nickel, Acta Mater. 207 (2021) 116702, https://doi.org/10.1016/j.actamat.2021.116702.
[54] Y. Wang, D. Raabe, C. Klüber, F. Roters, Orientation dependence of nanoindentation pile-up patterns and of nanoindentation microtextures in copper single crystals, Acta Mater. 52 (2004) 2229–2238, https://doi.org/10.1016/j.actamat.2004.01.016.
[55] L. Yin, O. Umezawa, Influence of dispersed β phase on local deformation pattern in mill-annealed Ti-Fe-O alloy under dwell fatigue loading, Int. J. Fatigue 152 (2021) 106447, https://doi.org/10.1016/j.ijfatigue.2021.106447.